Dynamic rupture inversion on the M5.9 pre-event before the 2024 M7.6 Noto-Peninsula, Japan, earthquake

Hideo Aochi

Earth, Planets and Space

FULL PAPER Open Access

Dynamic rupture inversion on the M5.9 pre-event before the 2024 M7.6 Noto-Peninsula, Japan, earthquake

Hideo Aochi[1,2*]

Abstract

Active seismicity, which began since late 2020 under the Noto Peninsula, Japan, led to the M7.6 earthquake on the 1st January 2024. This paper analyzes the M5.9 pre-event that occurred 13 s before the M7.6 mainshock. Near-field ground motion records clearly distinguish this pre-event from the ground shaking of the mainshock. We then use six near-field ground motions over a 10-s period to obtain first the focal mechanism and then dynamic rupture models by fixing the hypocenter location. We obtain a steep dip angle of 67°, whereas the dip of the M7.6 mainshock is 33° after Japan Metrological Agency catalog. We propose a simplified inversion process that dynamic rupture models are built by varying the location of the target circular patch, the stress level and the fault dipping directions. The preferred model has an up-dip rupture directivity (rake direction) on the south–east dipping fault, i.e. propagating away from the hypocenter of the M7.6 mainshock, and the two events are not aligned on the same planar fault. Uplift of about 20 cm and more is expected on the north coast of the Noto Peninsula in the case of the stress drop of 6 MPa or less. We also analyze another M5.5 pre-event 4 min earlier, with a slightly deeper focal depth and a gentle dip angle of 36°. This earthquake has also a rupture directivity in the up-dip direction. This infers that there should have been a preparation process of the M7.6 mainshock behind these pre-events and multiple fault segmentations around the hypocenter zone might have played a role.

Keywords 2024 Noto Peninsula earthquake, Pre-events, Dynamic rupture process, Near-field ground motions

*Correspondence:
Hideo Aochi
aochi.hideo@gmail.com
Full list of author information is available at the end of the article

Graphical Abstract

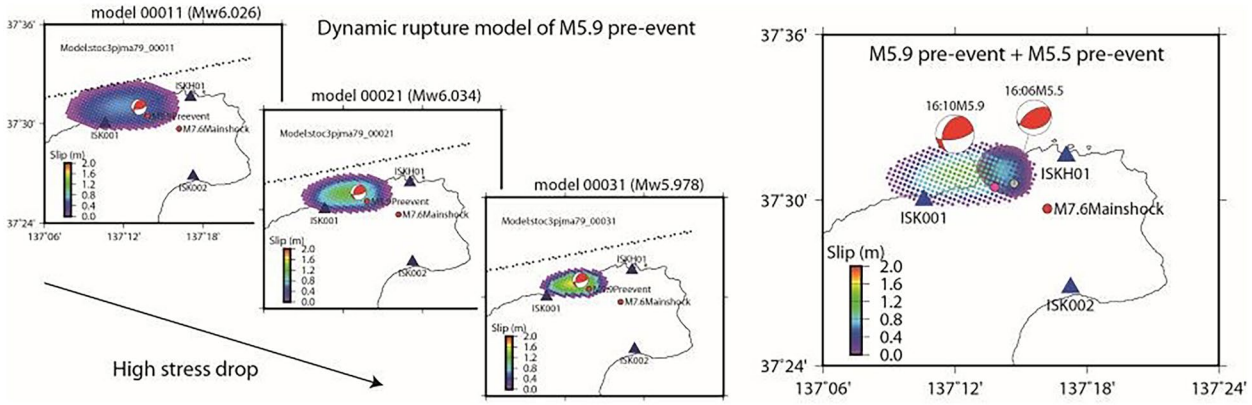

1 Introduction

The initiation process of earthquakes is the subject of long debate, whether it involves nucleation or a cascade rupture (e.g., Ellsworth and Beroza 1995). Some earthquakes reveal foreshock activities, indicating the acceleration of such an initiation process prior to large earthquakes (Bouchon et al. 2011; Kato et al. 2012; Ruiz et al. 2014; Ellsworth and Bulut 2018). This process is referred to as nucleation (Dieterich 1992; Matsu'ura et al. 1992), in which pre-slip zone becomes large enough to reach the critical size and then begins to propagate further along the fault plane. Thus, the initiation process, known as nucleation, is included in the mainshock rupture process. Some foreshocks are expected to occur in the nucleation zone, reflecting the extension of the nucleation zone (Kato et al. 2012). This nucleation process can take place both quasi-statically, or even dynamically. In the latter case, the critical size depends on the rupture velocity in the nucleation zone (Uemura et al. 2023). On the other hand, some earthquakes involve pre-events, which may not be part of the mainshock in space, and which is considered to be different from its nucleation process. In the case where a pre-event occurs just before the mainshock, the seismic wave radiation is hidden by the waves of the mainshock and can only be identified at certain near-field seismic stations. For example, the 2015 Mw8.3 Illapel earthquake (Ruiz et al. 2016; Aochi and Ruiz 2021) may have a pre-event of Mw 6.8–6.9 about 20 s before the mainshock. According to kinematic and dynamic rupture models, this pre-event area is not included in the ruptured area of the mainshock, whose nucleation would have had to be prepared differently elsewhere.

The January 1st 2024 M7.6 (Mw7.5 after CMT solution of JMA) Noto Peninsula earthquake occurred after continuous seismicity since late 2020, as previously studied by many groups, including Amezawa et al. (2023), Yoshida et al. (2023), Nishimura et al., (2023) and Kato (2023). The coseismic process of the M7.6 mainshock has been extensively studied and reported together 2 weeks after the mainshock by the Headquaters for Earthquake Research Promotion under the Prime Minister's Office in Japan (https://www.jishin.go.jp). All the ruptured fault segments of M7.6 earthquake correspond to the fault structure known for a 150 km-length from geophysical survey (e.g. Okamoto 2019; Okamoto et al. 2024). In detail, Asano and Iwata (2024) suggest that the rupture process have two stages, namely, the first rupture propagating south–west and the second north–east, and that their segments may be different. Indeed, the Japan Meteorological Agency publishes the homogeneous catalog of seismicity in Japan, and distinguishes two earthquakes with a delay of 13 s:

- Date Time (JST) Latitude Longitude Depth Magnitude
- 2024/01/01 16:10:09.5 37°30.4′N 137°13.8′E 10 km M5.9
- 2024/01/01 16:10:22.5 37°29.7′N 137°16.2′E 16 km M7.6

Two earthquakes are close enough, as shown in Fig. 1. Hereafter, we refer to them as M5.9 pre-event and M7.6 mainshock. The seismic wave radiation from the M5.9 pre-event is clearly distinguishable from the mainshock ground shaking only at the three nearest stations, ISKH01, ISK001 and ISK002, located a

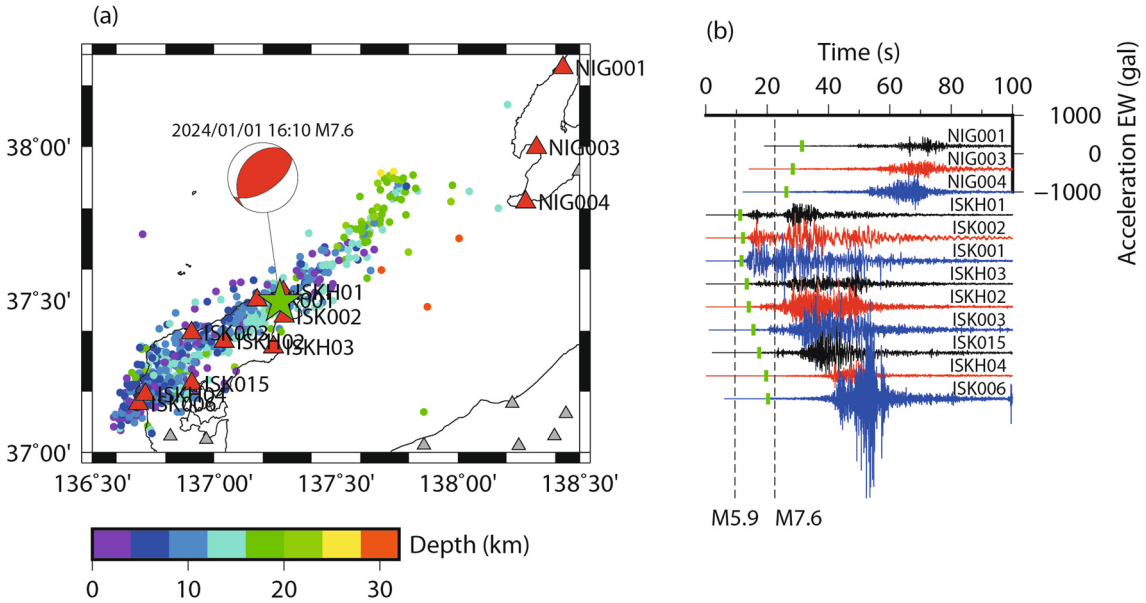

Fig. 1 **a** Map around the 2024/01/01 Noto Peninsula earthquake. The focal mechanism is obtained from F-NET (NIED) and the 1-day seismicity of the 1st January 2024 is shown from the JMA catalog. The acceleration networks are from K-net and Kik-net (NIED). **b** Recorded accelerations of the east–west component at selected stations. Waveforms are aligned at 16:00:00. The origin times of M5.9 pre-event and M7.6 mainshock are indicated. The *green bar* indicates the P-wave arrival of M5.9 pre-event picked by the author. For Kik-net stations, the recording at depth is shown

few kilometers from the epicenter area. The aim of this study is to analyze the M5.9 pre-event to determine whether this is a nucleation process (foreshock) of the M7.6 mainshock. We perform a dynamic rupture inversion using the near-field ground motions to determine the ruptured area and rupture directivity.

The dynamic rupture inversion process has been applied to various earthquakes (e.g., Peyrat et al. 2001; Di Carli et al 2010; Ruiz and Madariaga 2011; Twardzik et al. 2014). Although the spatial resolution is limited compared to kinematic inversions, it is possible reveal the causality of rupture propagation from a starting point. Aochi and Twardzik (2020) analyzed the 2016 Amatrice, Italy, earthquake using a few near-field ground motion data, and were able to identify seismogenic asperities (patches responsible for seismic wave radiation) in a manner consistent with known kinematic models and the scaling relation between fracture energy and patch size (e.g., Ide and Aochi 2005). This process is applicable at the beginning of seismic signals, even if the entire rupture process is not yet complete. In this study, we adopt this previous approach to identify rapidly the causal asperity of the M5.9 pre-event without analyzing the M7.6 mainshock.

2 Data and focal mechanism

We focus on the M5.9 pre-event preceding the M7.6 mainshock. The focal mechanism of this pre-event has not been systematically obtained in the catalogs, so we first perform the focal mechanism inversion for a given hypocenter position (Aochi and Burnol 2018). We invert only five parameters: fault strike, dip, rake, time shift (t_0) and moment magnitude (M_w) through a genetic algorithm. As shown in Fig. 1, the waveform corresponding to the M5.9 pre-event is distinct from the M7.6 mainshock in the nearfield so we use only a fixed time window of 10 s to minimize the residual between synthetics and observations at the six selected stations. The residual is defined here as $\epsilon = \sum \left(y^{\mathrm{obs}}(t) - y^{\mathrm{syn}}(t) \right)^2$, where the sum is made over the three components and time steps included in the time window. We dare to use the absolute residual, because it is important information, indicating that the main ground motions have not yet arrived at the distant stations in our process, and also because the filter introduces oscillations into the observed waveforms regardless of this causality due to the strong motions of the mainshock. Synthetics are calculated using a finite difference method (Aochi and Madariaga 2003) in a 1D

structure model, used in this region by Nishimura et al. (2023). We filter both synthetics and observations between 0.05 and 0.5 Hz.

We test seven epicenter positions and different focal depths, according to the probable earthquake locations from different resources (Fig. 2). Positions #2 and #5 are the epicenters of the M7.6 mainshock and M5.9 pre-event in the JMA catalog. The result of focal mechanism inversion is summarized in Fig. 3. We do not see clearly the residual minimum (see another example in discussion), mainly because the data available for this analysis are limited and may be contaminated by the subsequent rupture process. Nevertheless, we observe the trend of the solution. Position #2 (M7.6 mainshock epicenter) shows poor convergence. For the other positions, a shallow focal depth enables better convergence. This suggests that the rupture process may have happened near station ISK001, as the ground shaking is the biggest before the 7.6 mainshock. However, as the ground shaking is significant (20 cm/s after the bandpass filter between 0.05 and 0.5 Hz), it is questionable whether this station suffers from a non-linear site effect. For further analysis of dynamic rupture inversion, we select two solutions at positions #5 (focal depth 12 km) and #7 (focal depth 6 km), which are the local minima in each analysis. The focal mechanisms obtained are very similar: (strike, dip, rake) = (N69°E, 65°, 104°) for position #5, and (N79°E, 67°, 121°) for #7, respectively. Position #7 corresponds to the position of the maximum slip in the following dynamic rupture inversion. We observe that the estimated magnitude also has a trend a function of focal depth. To set up the dynamic rupture inversion, we target a moment magnitude Mw6.0, corresponding to that at the focal depth of 10 km.

3 Dynamic rupture inversion

The aim of dynamic rupture inversion is to gain a better understanding the causality of the rupture process not only in spatio-temporal evolution but also in stress condition. Let us suppose that the rupture process is governed by linear slip-weakening friction (Fig. 4). The fault strength is defined as a function of on-going slip Δu as follows:

$$\tau(\Delta u) = \tau_r + \Delta\tau_b \left(1 - \frac{\Delta u}{D_c}\right) H\left(1 - \frac{\Delta u}{D_c}\right)$$

where the breakdown strength drop $\Delta\tau_b$ is the difference between the peak strength τ_p and the residual strength τ_r, namely, $\Delta\tau_b \equiv \tau_p - \tau_r$. $H(\cdot)$ is the Heaviside function, as $H(x \geq 0) = 1$ or $H(x < 0) = 0$. We consider a planar fault in an infinite homogeneous medium, so that normal stress play no explicit role and $\tau_r = 0$ can be assumed without loss of generality. The parameter D_c is called the

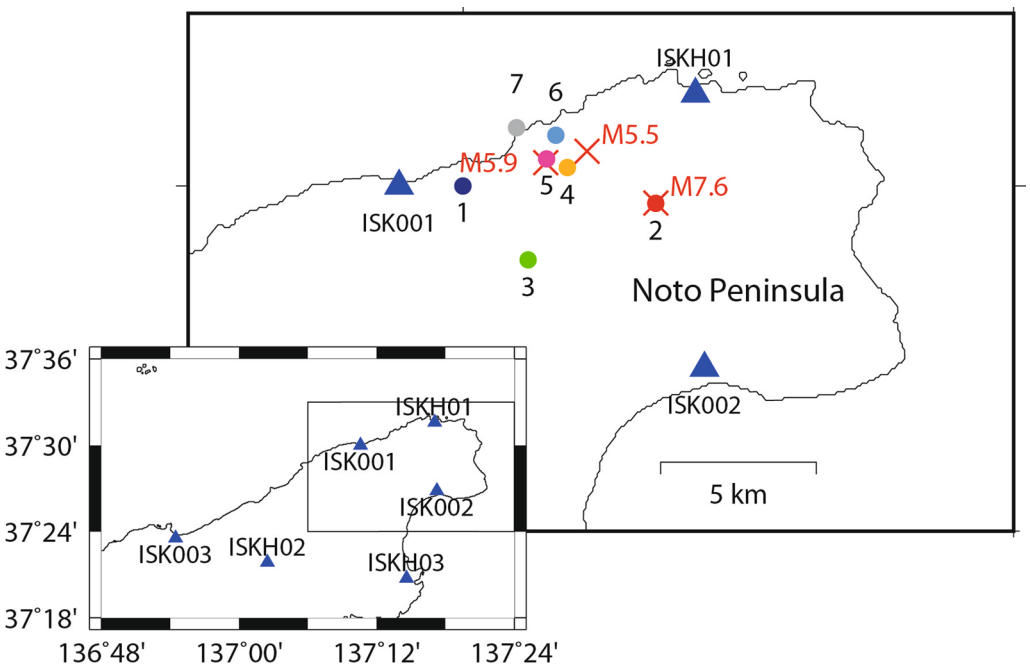

Fig. 2 Map around the epicenters of the Noto earthquakes. The *numbered circle* points indicate the position tested for focal mechanism inversions. The crosses are the epicenters of the 16:06 M5.5, 16:10 M5.9 and 16:10 M7.6 earthquakes from the JMA catalog. The triangles are the locations of the K-net and Kik-net stations

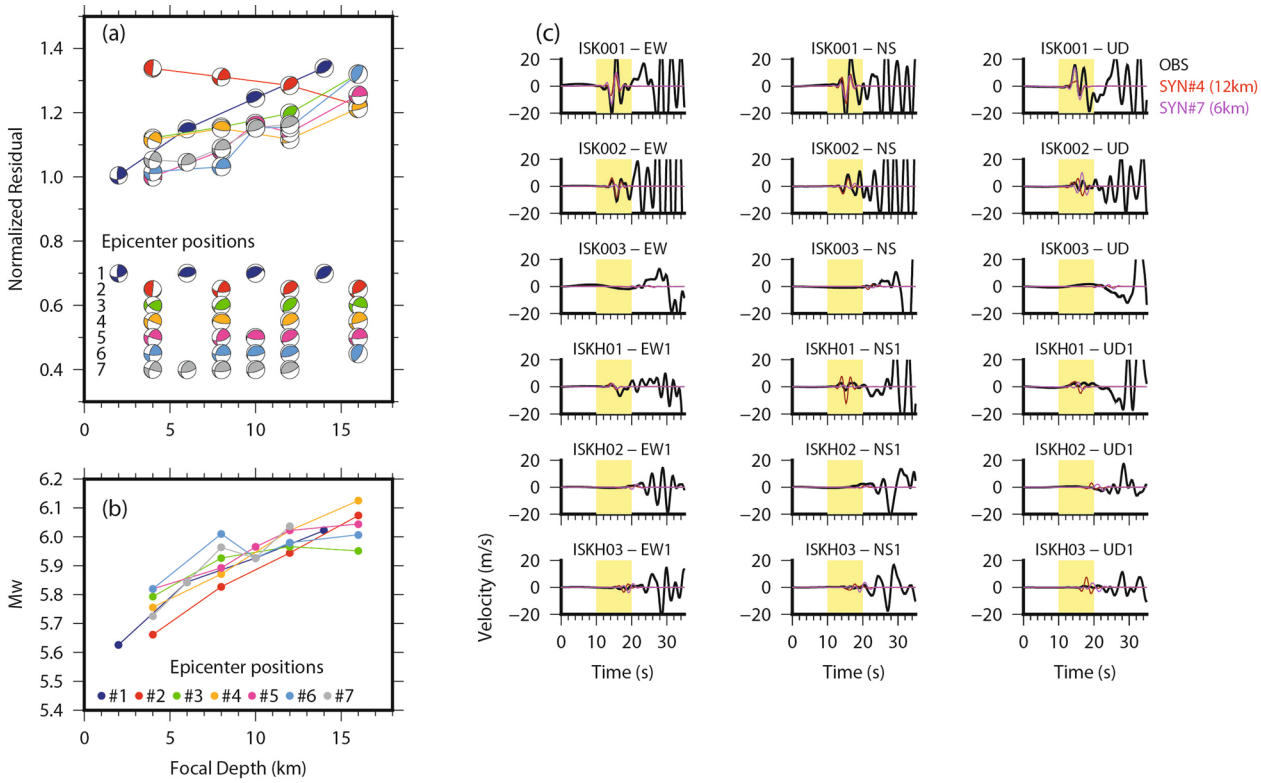

Fig. 3 Fault mechanism inversion for the 16:10 M5.9 pre-event. Different epicenter positions are tested and their locations are shown in Fig. 2. **a** Focal mechanism obtained for different focal depths. **b** Moment magnitude (M_w) obtained for different focal depths. **c** Comparison between observation and synthetic waveforms, filtered between 0.05 and 0.5 Hz. Two synthetics are selected. Epicenter position #4 with a focal depth of 12 km, and #7 with a focal depth of 6 km

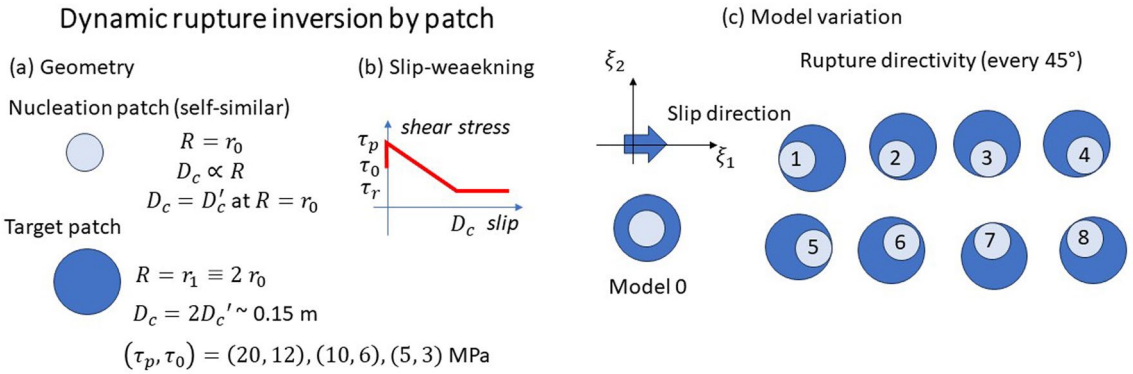

Fig. 4 Inversion setup of dynamic rupture by patch. **a** We adopt the target patch size to obtain a consistent seismic moment already known. Three stress conditions are tested. It is assumed that the nucleation patch is half the target patch and critical slip displacement D_c increases linearly with the epincentral distance R. **b** Slip-weakening friction. Peak strength, initial shear stress and residual stress are τ_p, τ_0 and τ_r, respectively. **c** Nine target patch positions are tested by fixing the nucleation patch. The local coordinate (ξ_1, ξ_2) is fixed to the slip direction, namely, slip Δu is in the ξ_1 -direction

critical slip displacement, characterizing the slip-weakening friction, and generally considered to be scale-dependent (Ohnaka 2003; Aochi and Ide 2004). The initial shear stress τ_0 is set, such that $\tau_0 < \tau_p$. The rupture stability is often examined using non-dimensional parameters, such as the S value (Das and Aki 1977) or κ (Madariaga and Olsen 2000):

$$S = \frac{\tau_p - \tau_0}{\tau_0 - \tau_r} \text{ and } \kappa = \frac{(\tau_0 - \tau_r)^2}{G(\tau_p - \tau_r)} \frac{L}{D_c}$$

where G is the rigidity of the medium and L is a characteristic length of the rupture process on a causal fault.

We prepare a small nucleation patch and a larger target patch to describe fault heterogeneity, similar to previous works (Aochi and Twardzik 2020; Aochi and Ruiz 2021). They are circular with radii $R = r_0$ and $R = r_1$, respectively, for simplicity. We seek to determine the relative position and frictional parameters of the target patch (Fig. 4), on which uniform frictional parameters (D_c, τ_p, τ_r) are assumed. On the other hand, for the nucleation patch, we assume that its size is equal to half of the target, $r_1 = 2r_0$ and that D_c is proportional to the distance from the center (Aochi and Ide 2004; Uemura et al. 2023). Consequently, the value of D_c on the target patch is twice that at the edge of the nucleation patch. Outside of the patches, no weakening, $\tau_r = \tau_p$, is supposed to gradually halt the rupture propagation. We then limit the number of simulations by discretizing key parameters in advance. We test three combinations of (τ_p, τ_0) and nine relative locations of the target patch with respect to the given nucleation patch, while following the D_c-scaling adopted in Ide and Aochi (2005) and Aochi and Twardzik (2020). Numerical simulations of the dynamic rupture process are carried out using boundary integral equation method (Aochi et al. 2000) and renormalization technique (Aochi and Ide 2004). The simulation starts with a grid size of $\Delta s = 32$ m for a fault size of 2048 m × 2048 m, and when the rupture reaches at the edge of the model dimension, it is normalized to a larger scale by a factor of 4, i.e., to $\Delta s = 128$ m and again to $\Delta s = 512$ m. The radius of the target patch r_1 is adjusted to obtain the magnitude expected to Mw6, i.e., $r_1 = 2.95$, 3.93 and 4.92 km for the high, (τ_p, τ_0) = (20 MPa, 12 MPa), medium, (τ_p, τ_0) = (10 MPa, 6 MPa), and low stress, (τ_p, τ_0) = (5 MPa, 3 MPa), cases, respectively, by keeping the same S value ($S = 0.67$). However these represents different values of κ, $\kappa = 1.82$, 2.91 and 4.37, respectively, letting $L = r_1$ and assuming $G = 32.4$ GPa in the above equation. The condition $\kappa > 1$ indicates that dynamic rupture propagation is favored over the assumed patch surface, as required. Synthetic seismograms are calculated on the basis of dynamic rupture source models using a finite difference method (Aochi and Madariaga 2003) supposing a regional 1D structure (Nishimura et al. 2023).

Figure 5 shows the comparison of the simulated slip area for the nine different target patch positions in the case of (τ_p, τ_0) = (10 MPa, 6 MPa). The magnitude ranges from Mw 5.98 (case 00020) to Mw6.04 (case 00022, 00024, 00026 and 00028). Seismograms from the six stations are compared in Fig. 6. As in the focal mechanism inversion, we use only the beginning of the waveforms for 10 s in the frequency range between 0.05 and 0.5 Hz. Here, we test two possible fault planes (southeast or northwest dipping), three stress levels and nine target patch locations. We run the procedure twice, i.e., using the two different locations (#4 and #5 in Fig. 2) and two slightly different focal mechanisms. The focal mechanism of the second run is the one obtained at position #7, where the maximum slip is obtained in the model 00021 of the first run. The trend in solution convergence is very similar. In general, convergence is better when the stress level is high, namely, the ruptured area is smaller, and when the rupture directivity is the same as the rake direction (numbered as model 11, 21, 31). Overall, models 00021 and 00031 of the southeast dipping fault are the two best, indicating a relatively higher stress drop and a localized ruptured area.

Figure 7 compares the vertical displacement at station ISK001 at which a temporal GPS station has been installed nearby showing uplift of about a few tenths' centimeters before the arrival of the mainshock deformation (Nishimura et al. 2024). It is briefly confirmed by the double integration of the acceleration data. However, the acceleration data may be subject to drift and do not show the final stable displacement after the arrival of the strong ground shaking from the M7.6 mainshock. For this reason, static displacement is not used in the previous inversion. However, from a qualitative point of view, the high-stress model does not retain sufficient final displacement, because the ruptured area is small, namely, far from station ISK001. Only the two models of low and medium stress values with the appropriate directivity can leave the final displacement of 20 cm, which is consistent with the insight from GPS measurements.

4 Discussion

The dip angle of the mainshock is obtained as 37° from JMA (e.g. Aoki et al. 2024). The aftershock distribution globally shows a gentile dip angle of about 20°–45° (e.g. Aoki et al. 2024; Matsubara and Sato 2024; Kato et al. 2024). In published finite-source models of the M7.6 mainshock, relatively small dip angles are adopted, for example, 37° in Aoki et al. (2024), 40°–54° in Nishimiya (2024), 35°–42° in Kurahashi et al. (2024). This reflects the spatial distribution of the aftershocks over the entire area. Guo et al. (2024) consider a dip variation up to 60° in the shallow part to be consistent with the known position of the active faults. To account for significant amount of uplift on the Noto Peninsula, the dip angle should be steeper, e.g. 50°–60° (Fujii and Satake 2024), 50° (Kubo et al. 2024), 40°–55° (Takamatsu et al. 2024). Yamada et al. (2024) propose a dip-variation model from 25° at depth to 60° at shallow depth. The

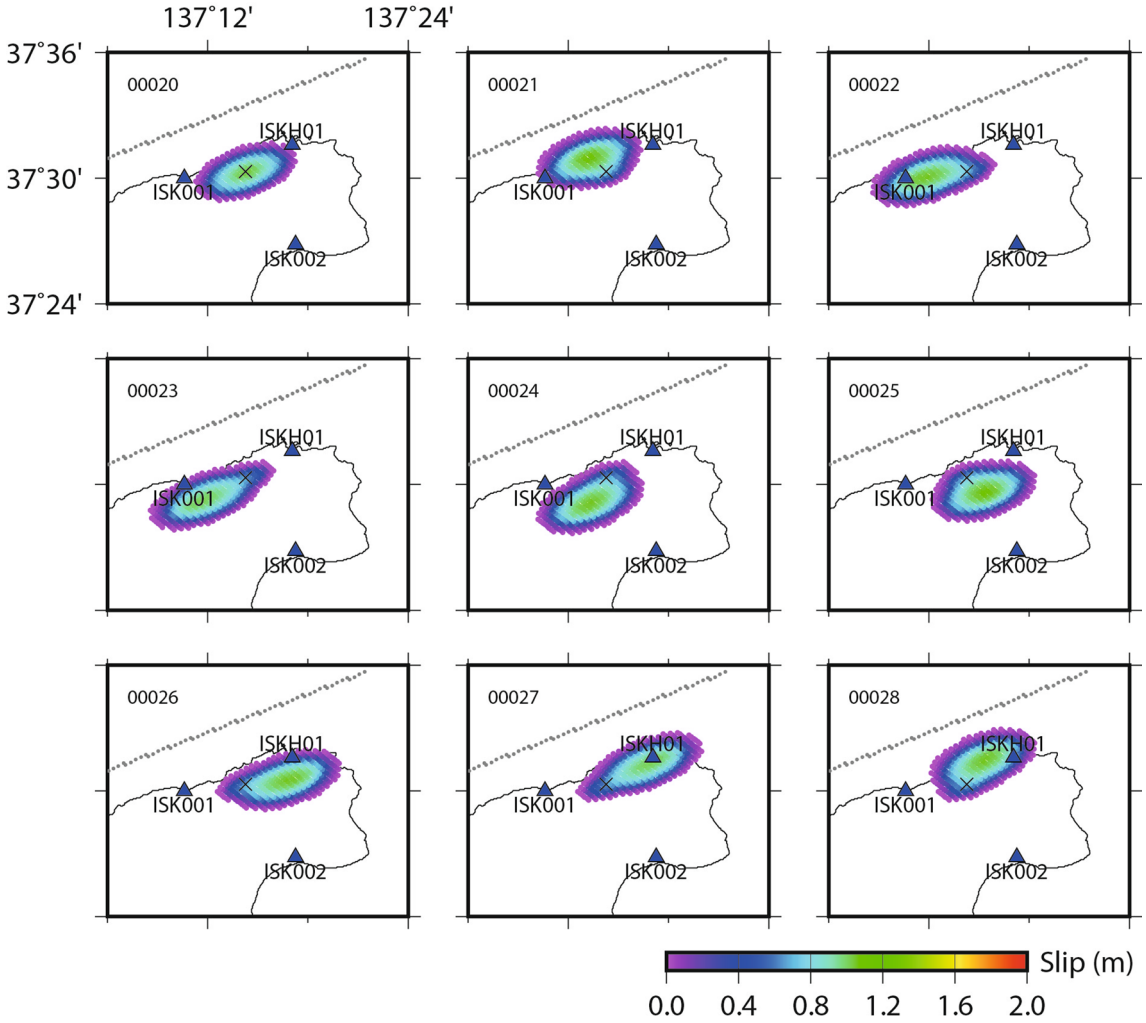

Fig. 5 Examples of dynamic rupture simulations projected on the map. The final slip distribution is shown with the nucleation point (cross) corresponding to the position number 4 in Fig. 2. The fault mechanism assumed here is (strike, dip, rake) = (69°, 65°, 104°), a southeast-dipping fault. *Grey dots* correspond to computational elements with depths less than 0.5 km, namely, the extension of the causal fault plane to the ground surface. (τ_p, τ_0) = (10 MPa, 6 MPa) and r_1 = 3.93 km

dip variation from depth to the surface can be geologically consistent with the known database (e.g. https://www.jamstec.go.jp/offshorefault/fault_model.html) and has been inferred within the schematic cross-sectional interpretations (e.g. Nishimura et al. 2023; Kato 2023). Here, we test the sensibility of the dynamic rupture inversion by setting the fault parameters (strike, dip, rake) = (N56°E, 33°, 125°). Figure 8 shows the results of dynamic rupture inversion. Overall, the convergence is worse than that of the previous solution with a dip of 67°. The ruptured area of a better solution extends far to the northwest under the sea. However, the final vertical displacement at ISK001 does not reach 10 cm, much smaller than the expected value (Fig. 7). This test therefore supports a high dip angle of this pre-event.

In the JMA catalog, another large event is reported before the M7.6 mainshock.

- Date Time (JST) Latitude Longitude Depth Magnitude
- 2024/01/01 16:06:06.1 37°30.6′N 137°14.7′E 12 km M5.5

The epicenter location is sufficiently close to the M5.9 pre-event, and we aim to analyze it in terms of focal mechanism and dynamic rupture inversion. We then use the same six stations and apply the same procedure. Figure 9 shows the focal mechanism result. We adopt a bandpass filter between 0.1 and 0.3 Hz and a duration of 15 s. The better solution is obtained for the focal depth

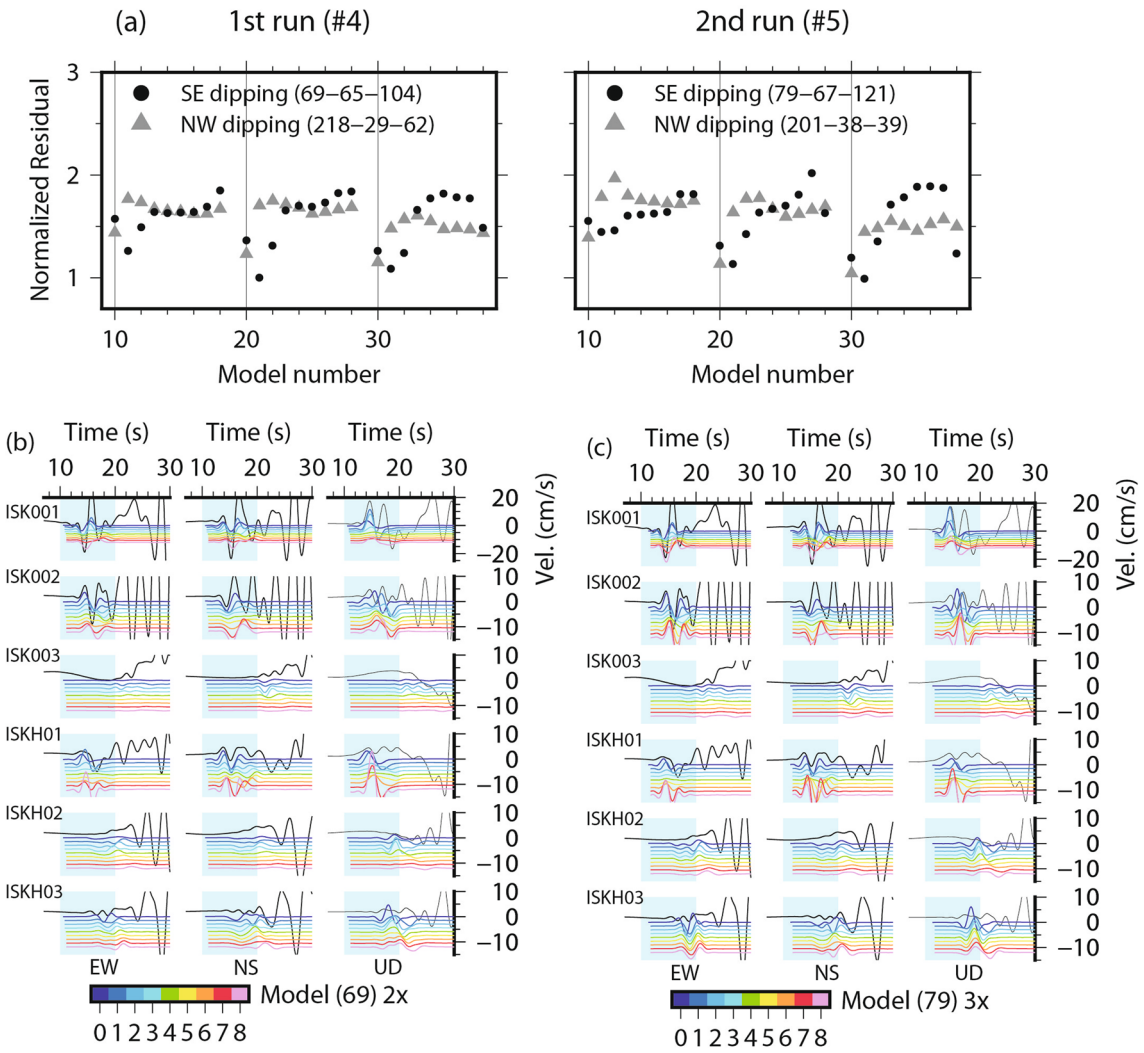

Fig. 6 Result of dynamic rupture inversion for the M5.9 pre-event. **a** Residuals between synthetics and observations. The first run defines the nucleation point as #4 (Fig. 2). Model numbers 1×, 2× and 3× represent the different stress levels $\tau_0 = 3$, 6, and 12 MPa, respectively, and $x = (0, 8)$ corresponding to the positions (Fig. 4). The second run sets the nucleation point at #5 (Fig. 2) with the focal mechanism obtained at #7, where the fault slip is the maximum in the model 21 of the southeast-dipping fault during the first run. **b** Fitting for models 2× of the southeast-dipping fault during the first run. **c** Fitting for models 3× of the southeast-dipping fault during the second run. Waveforms are filtered between 0.05 and 0.5 Hz and the period between 10 and 20 s is used for residual calculations

set at 8 km, and the focal mechanism obtained is (strike, dip, rake) = (N81°E, 36°, 110°) and $M_w = 5.3$. This solution is similar to the one obtained by F-NET (N58°E, 44°, 90°) and $M_w = 5.3$, although they do not use the near-field stations. An uncertainty of about 20° remains, but the dip angle is clearly small compared with the previous analysis. Next, we perform dynamic rupture inversion. Figure 10 summarizes the solution obtained together with the M5.9 pre-event. In terms of residual, there is no significant preference of the fault plane direction, however, it is known that southeast-dipping faults are dominant in the area from the seismological analyses. The preferred stress level of the M5.5 pre-event is higher than the other, probably because the focal depth is deeper. The ruptured areas of the two pre-events are superposed on the map, however they have different focal depths and fault dips. The two fault planes therefore dot not intersect. Both rupture processes show a preference of rupture extension to the northwest, i.e. from deep to shallow. This also means that the pre-events do not contain the hypocenter area of the M7.6 mainshock and are getting away from it, as seen on the cross section. This suggests that stress is concentrated at depth and that various fault systems have attempted to release the energy toward the surface.

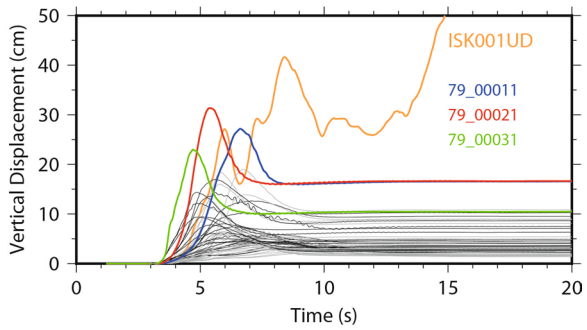

Fig. 7 Comparison of the vertical displacement at station ISK001. The signals are aligned to the origin time 16:10:9.5. The observation waveform (*orange*) is integrated twice without filtering from the acceleration data. All the results from the second run (strike N79°E and N201°E) are shown in *black*. Three models are shown in color, model 00011, 00021 and 00031 for the strike N79°E of a southeast-dipping fault

In Fig. 11, we calculate the evolution of dynamic stress at the position of the M7.6 hypocenter supposing the fault mechanism of (strike, dip, rake) = (N52°E, 42°, 90°), according the source model of Asano and Iwata (2024). We observe the dynamic perturbation reaches around 0.4 MPa from M5.5 event, larger than that of M5.9 event. This is explained by the fact that the extended source area is closer and stress drop is larger for the M5.5 event. On the other hand, the change in static stress is around 0.1 MPa from the M5.9 event, larger than the M5.5 event, because the extended source area is bigger. Thus, although there is still a possibility of remote triggering, another appropriate nucleation process is required for the M7.6 mainshock, different from these pre-events. Finally, from a mechanical point of view, it is reasonable to distinguish the M5.9 pre-event from the M7.6 mainshock on the seismicity catalog.

The dynamic rupture model in this study remains the first approximation of the rupture process to determine the characteristic behavior of the process, such as the ruptured area and rupture directivity, from the relatively low-frequency range (0.05 and 0.5 Hz) of the near-field ground motion data (Fig. 6). However, in the unfiltered observation at ISK001 in Fig. 7, we observe the first peak at about 5.5 s, and the second one at 8.5 s, whereas all the synthetics have one peak, corresponding to one target patch in the model setup. It remains possible that the rupture process of M5.9 pre-event continues, triggering another nearby zone in cascade. ISK001 is the closet station from which to discuss the detail process from the pre-event to the mainshock rupture. Asano and Iwata (2024) do not include ISK001 in their finite-source inversion, in which two different parallel segments are considered and the M5.9 pre-event and M7.6 mainshock start either of the segments independently. In their analysis, it appears that the M5.9 event has already two asperities in the first 10 s and continues to propagate south–westwards during 40 s, while the M7.6 mainshock concerns the rupture propagation north–eastwards on a different fault structure. Thus, the rupture process could have been more complex than our dynamic rupture simulation which could have realized the first characteristic asperity (rupture patch) only. However, our results are consistent with their interpretation in the sense that M5.9 pre-event and M7.6 mainshock should have separately driven different faults. This suggests the important role of multiple segments in the earthquake initiation process.

5 Conclusion

In this paper, we analyzed two moderate pre-events (M5.5 an M5.9), which, respectively, occurred 4 min and 13 s before the M7.6 Noto Peninsula, Japan, earthquake

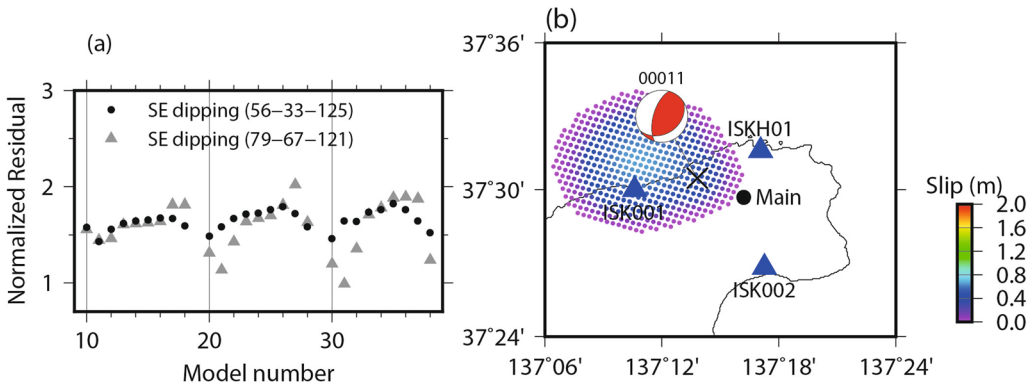

Fig. 8 Dynamic rupture inversion result for the fault parameter (strike, dip, rake) = (N56°E, 33°, 125°). **a** Normalized residual over the same six stations. For reference, the previous solution (Fig. 5) for parameters (strike, dip, rake) = (N79°E, 67°, 121°) is also shown. **b** Ruptured area for a better model 00011. The hypocenter position is supposed on a *cross mark*

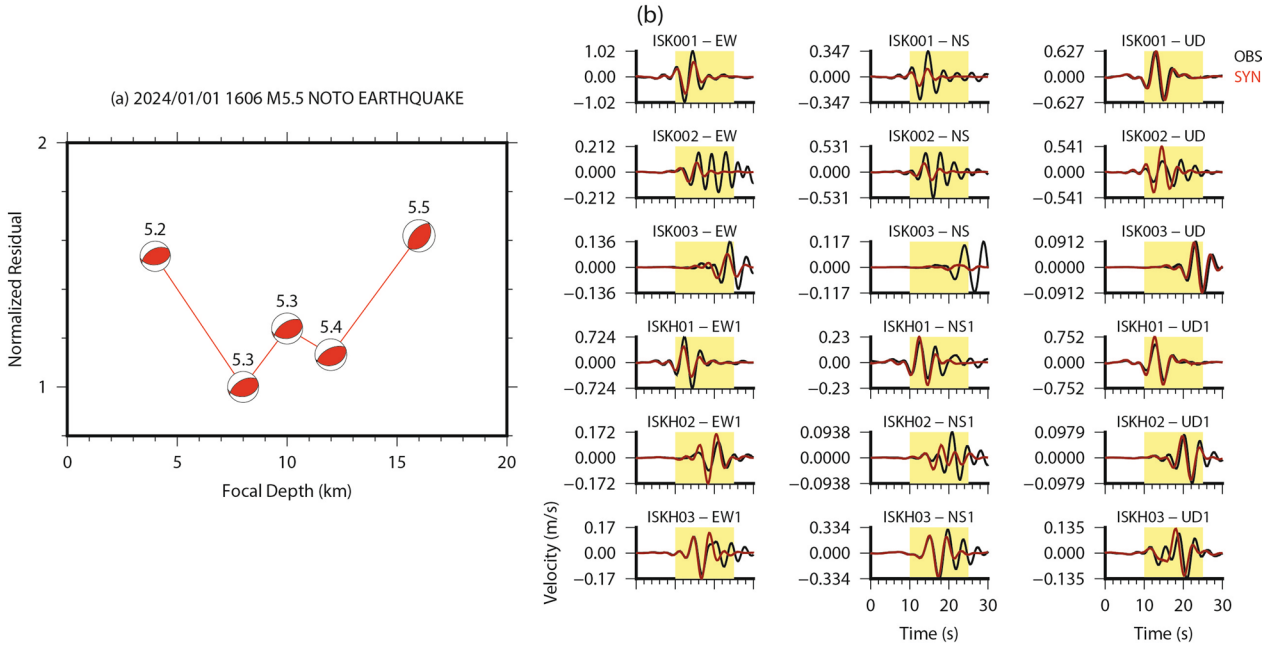

Fig. 9 Focal mechanism inversion for the M5.5 pre-event. **a** Test for different focal depths. The number indicates the moment magnitude obtained. **b** Comparison of synthetic and observed seismograms at six stations for a focal depth set at 8 km. Only a 15-s duration (*yellow part*) is used for inversion. Waveforms are filtered between 0.1 and 0.3 Hz

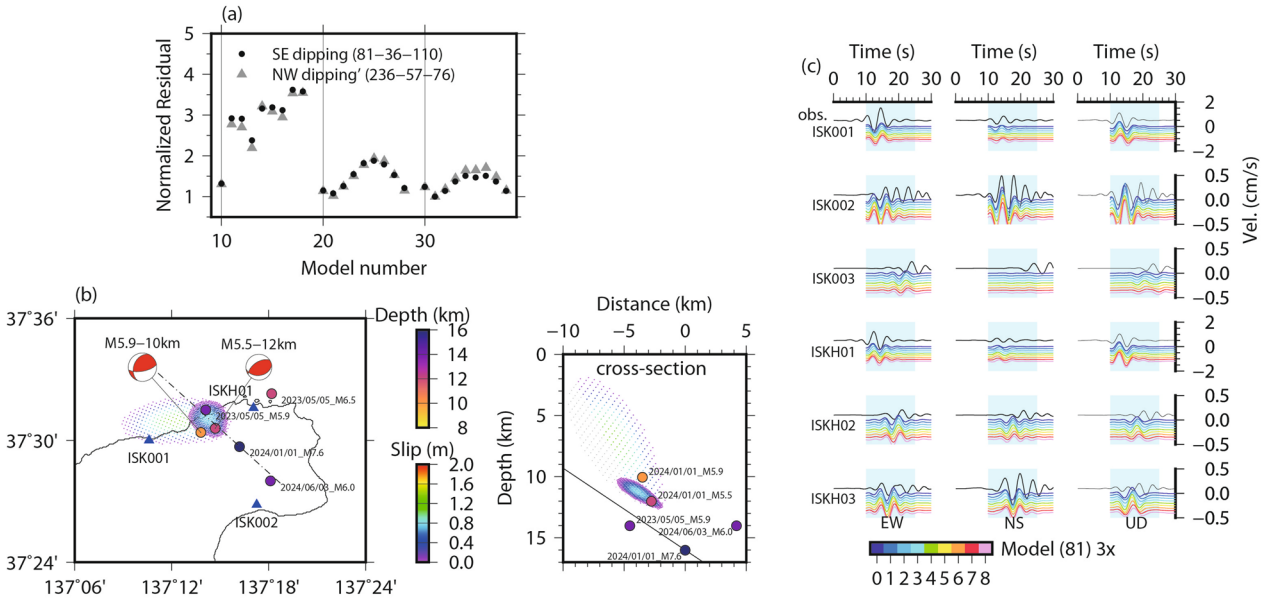

Fig. 10 Dynamic rupture inversion results for the M5.5 pre-event. **a** Normalized residual for fixed fault parameters. See also Fig. 6 caption. **b** Ruptured area obtained for a better model 00031 (southeast-dipping fault, with a high stress case). **c** Comparison between observed (in *black*) and synthetic (in *color*) waveforms filtered between 0.03 and 0.3 Hz. Models from 00030 to 00038 on a southeast-dipping fault with a high stress case are shown. A 15-s section is used to calculate residuals

on the 1st January 2024. The seismic waves of M5.9 pre-event are distinguishable from the ground shaking of the M7.6 mainshock at the nearest stations. We used six near-field ground motions over a 10-s period to obtain first the focal mechanism and then dynamic rupture models by fixing the hypocenter location. Dynamic

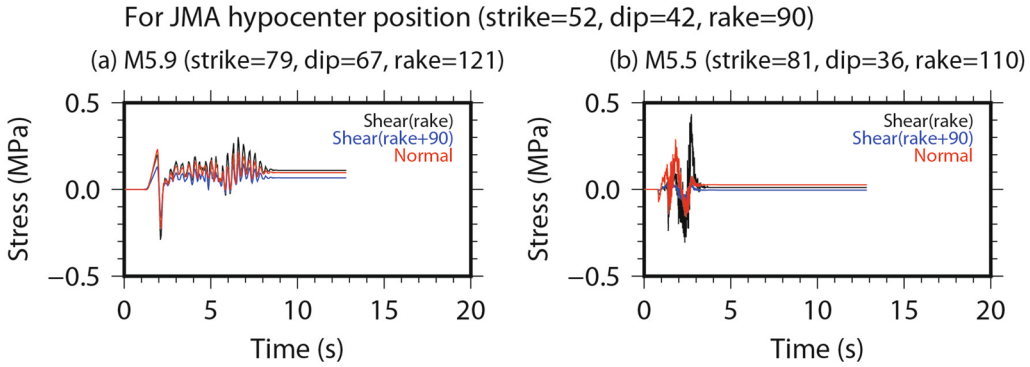

Fig. 11 Stress change at the hypocenter position of M7.6 mainshock assuming the fault mechanism of (strike, dip, rake) = (N52°E, 42°, 90°) from **a** M5.9 pre-event and **b** M5.5 pre-event. Three components of stress on the supposed fault plane are calculated

rupture models are built by varying the location of a target circular patch relative to the nucleation patch. This simple description makes it possible to explore the rupture characteristics rapidly with observations. For a given focal mechanism, we performed 54 dynamic rupture models (nine positions, three stress levels and two fault orientations) every time. We have obtained that the M5.5 pre-event has a dip of 36° at a focal depth of 12 km (Mw5.3) and the M5.9 has 67°-dip at 10 km depth (approximatively Mw6.0). Both pre-events have a preferential rupture directivity to the up-dip (rake) direction on a southeast-dipping fault, i.e. propagating away from the hypocenter of the M7.6 mainshock. The M5.9 pre-event is not aligned on the same planar fault as the M7.6 mainshock. This infers that M5.9 pre-event is not part of the nucleation process of M7.6 mainshock and there should have been another intrinsic preparation process behind these pre-events. Multiple fault segmentations around the hypocenter zone might have played a role.

Abbreviations

JMA Japan Meteorological Agency, Japan
NIED National Research Institute for Earth Science and Disaster Resilience, Japan

Acknowledgements

I thank for the data available from National Research Institute for Earth Science and Disaster Resilience and Japan Meteorological Agency. I also thank for the colleagues from both institutions and from the Disaster Prevention Research Institute of Kyoto University and the Earthquake Research Institute of the University of Tokyo for the fruitful discussions and information exchange. I also thank two anonymous reviewers and Dr. Haruko Sekiguchi for careful reviews and suggestions.

Author contributions

I have worked from the conception to the paper writing.

Funding

All the simulations are held at the French national computing centre GENCI/Idris and GENCI/TGCC under grant A0150406700. This work is a contribution to the project 'E-CITY' (Near-fault observation and simulation of earthquake ground motion in an urban environment) funded by the Agence Nationale de la Recherche of France (ANR-21-CE22-0020).

Availability of data and materials

The ground motion data (K-net and Kik-net) and focal mechanism (F-net) are available from National Research Institute for Earth Science and Disaster Resilience (https://www.kyoshin.bosai.go.jp/kyoshin/ and https://www.hinet.go.jp/topics/noto240101/). Seismicity catalog is available from Japan Meteorological Agency (https://www.data.jma.go.jp/eqev/data/daily_map/index.html). A boundary integral equation method and a finite difference code is available on line by the author (doi: https://doi.org/10.5281/zenodo.1472238 and https://zenodo.org/records/10225172). A genetic algorithm utility library is available from http://gaul.sourceforge.net.

Declarations

Ethics approval and consent to participate

Not applicable.

Consent for publication

Not applicable.

Competing interests

Not applicable.

Author details

[1]Bureau de Recherches Géologiques et Minières, Orléans, France. [2]Laboratoire de Géologie de l'Ecole Normale Supérieure, CNRS UMR 8538, PSL Research University, Paris, France.

Received: 2 June 2024 Accepted: 27 October 2024
Published online: 20 November 2024

References

Amezawa Y, Hiramatsu Y, Miyakawa A, Imanishi K, Otsubo M (2023) Long-living earthquake swarm and intermittent seismicity in the Northeastern tip of the Noto Peninsula, Japan. Geophys Res Lett 50:e2022GL102670. https://doi.org/10.1029/2022GL102670

Aochi H, Burnol A (2018) Mechanism of the ML4.0 25th April 2016 earthquake in southwest of France in the vicinity of the Lacq gas field. J Seismol 22:1139–1155. https://doi.org/10.1007/s10950-018-9758-5

Aochi H, Ide S (2004) Numerical study on multi-scaling earthquake rupture. Geophys Res Lett 31:L02606. https://doi.org/10.1029/2003GL018708

Aochi H, Madariaga R (2003) The 1999 Izmit, Turkey, earthquake: non-planar fault structure, dynamic rupture process and strong ground motion. Bull Seism Soc Am 93:1249–1266. https://doi.org/10.1785/0120020167

Aochi H, Ruiz S (2021) Eartly stage and main ruptures of the 2015 Mw8.3 Illapel, Chile, Megathrust earthquake: kinematic elliptical inversions and dynamic rupture simulations. J Geophys Res 126:e2020JB021207. https://doi.org/10.1029/2020JB021207

Aochi H, Twardzik C (2020) Imaging of seismogenic asperities of the 2016 ML6.0 Amatrice, Central Italy, earthquake through dynamic rupture simulations. Pageoph 170:1931–1946. https://doi.org/10.1007/s00024-019-02199-z
Aochi H, Fukuyama E, Matsu'ura M (2000) Spontaneous rupture propagation on a non-planar fault in 3D elastic medium. Pure Appl Geophys 157:2003–2007. https://doi.org/10.1007/PL00001072
Aoki S, Oka T, Shimizu J, Kawai A, Moriwaki K, Kuwayama T, Yamada Y, Yurimoto G (2024) The 2024 Noto Peninsula earthquake -seismicity and earthquake/tsunami information issued by JMA. In: Abstract of Japan Geoscience Union Meeting 2024: U15-P01, Chiba, Japan, 26–31 May 2024
Asano K, Iwata T (2024) Source rupture process of the 2024 Noto Hanto earthquake by waveform inversion of strong motion records. In: Abstract of Japan Geoscience Union Meeting 2024: U15-P20, Chiba, Japan, 26–31 May 2024
Bouchon M, Karabulut H, Aktar M, Özalaybey S, Schmittbuhl J, Bouin MP (2011) Extended nucleation of the 1999 Mw7.6 Izmit earthquake. Science 331:877–880. https://doi.org/10.1126/science.1197341
Das S, Aki K (1977) A numerical study of two-dimensional spontaneous rupture propagation. Geophys J Royal Astr Soc 50:643–668. https://doi.org/10.1111/j.1365-246X.1977.tb01339.x
Di Carli S, François-Holden C, Peyrat S, Madariaga R (2010) Dynamic inversion of the 2000 Tottori earthquake based on elliptical subfault approximations. J Geophys Res 115:B12238. https://doi.org/10.1029/2009JB006358
Dieterich JH (1992) Earthquake nucleation on faults with rate- and state-dependent strength. Tectonophys 211:115–134. https://doi.org/10.1016/0040-1951(92)90055-B
Ellsworth WL, Beroza GC (1995) Seismic evidence for an earthquake nucleation phase. Science 268:851–855. https://doi.org/10.1126/science.268.5212.851
Ellsworth WL, Bulut F (2018) Nucleation of the 1999 Izmit earthquake by a triggered cascade of foreshocks. Nature Geos 11:531–535. https://doi.org/10.1038/s41561-018-0145-1
Fujii Y, Satake K (2024) Slip distribution of the 2024 Noto Peninsula earthquake (MJMA 7.6) estimated from tsunami waveforms and GNSS data. Earth Planet Space 76:44. https://doi.org/10.1186/s40623-024-01991-z
Guo Y, Miyakoshi K, Sato T (2024) Source process on variable-dip faults of the 2024 Noto Peninsula earthquake (M_J 7.6) inverted from strong-motion records. In: Abstract of Japan Geoscience Union Meeting 2024: U15-P34, Chiba, Japan, 26–31 May 2024
Ide S, Aochi H (2005) Earthquakes as multiscale dynamic ruptures with heterogeneous fracture surface energy. J Geophys Res 110:B11303. https://doi.org/10.1029/2004JB003591
Kato A (2023) Implication of fault-valve behabior from immediate aftershocks following the 2023 Mj6.5 earthquake benearth Noto Peninsula, Central Japan. Geophys Res Lett 51:e2023GL106444. https://doi.org/10.1029/2023GL106444
Kato A, Obara K, Igarashi T, Tsusuoka H, Nakagawa S, Hirata N (2012) Propagation of slow slip leading up to the 2011 Mw9.0 Tohoku-oki earthquake. Science 335:705–708. https://doi.org/10.1126/science.1215141
Kato A, Nakagawa S, Kurashimo E, Sakai S (2024) The long-lasting earthquake swarm leading up to the 2024 M7.6 Noto-Hanto earthquake, Japan. In: Abstract of Japan Geoscience Union Meeting 2024: U16-01, Chiba, Japan, 26–31 May 2024
Kubo H, Suzuki W, Aoi S, Sekiguchi H (2024) Source process of the 2024 Noto Peninsula earthquake derived from strong motion data. In: Abstract of Japan Geoscience Union Meeting 2024: U15-P36, Chiba, Japan, 26–31 May 2024
Kurahashi S, Miyakoshi K, Irikura K (2024) Estimation of source rupture process of the 2024 Noto-hanto earthquake sequence focusing on rupture propagation complexity. In: Abstract of Japan Geoscience Union Meeting 2024: U15-P27, Chiba, Japan, 26–31 May 2024
Madariaga R, Olsen KB (2000) Criticality of rupture dynamics in 3-D. Pure Appl Geophys 157:1981–2001. https://doi.org/10.1007/PL00001071
Matsu'ura M, Kataoka H, Shibazaki B (1992) Slip-dependent friction law and nucleation processes in earthquake rupture. Tectonophys 211:135–148. https://doi.org/10.1016/0040-1951(92)90056-C
Matsubara M, Sato H (2024) Seismic velocity structure along the source fault of the 2024 Noto Peninsula earthquake and aftershock distribution compared with the fault model. In: Abstract of Japan Geoscience Union Meeting 2024: U15-P08, Chiba, Japan, 26–31 May 2024
Nishimiya T (2024) The source process inversion of the 2024 Noto Peninsula earthquake on various fault plane models with local seismograms. In: Abstract of Japan Geoscience Union Meeting 2024: U15-P23, Chiba, Japan, 26–31 May 2024
Nishimura T, Hiramatsu Y, Ohta Y (2023) Episodic transient deformation revealed by the analysis of multiple GNSS networks in the Noto Peninsula, central Japan. Sci Rep 13:8381. https://doi.org/10.1038/s41598-023-35459-z
Nishimura T, Hiramatsu Y, Ohta Y (2024). Source models for the 2020–2024 Noto Peninsula earthquakes based on GNSS data. In: Abstract of Japan Geoscience Union Meeting 2024: U16-P02, Chiba, Japan, 26–31 May 2024
Ohnaka M (2003) A constitutive scaling law and a unified comprehension for frictional slip failure, shear fracture of intact rock, and earthquake rupture. J Geophys Res 108:2080. https://doi.org/10.1029/2000JB000123
Okamoto Y (2019) Distribution of active faults in Japan Sea and future issues. Zisin 71:185–199. https://doi.org/10.4294/zisin.2017-21
Okamoto Y, Inoue T, Sato T, Ogami T (2024) Relationship between offshore active faults around the Noto Peninsula and the 2024 Noto Peninsula earthquake. In: Abstract of Japan Geoscience Union Meeting 2024: U15-02, Chiba, Japan, 26–31 May, 2024
Peyrat S, Olsen KB, Madariaga R (2001) Dynamic modeling of the 1992 Landers earthquake. J Geophys Res 106:26467–26482. https://doi.org/10.1029/2001JB000205
Ruiz S, Madariaga R (2011) Determination of the friction law parameters of the Mw 6.7 Michilla earthquake in northern Chile by dynamic inversion. Geophys Res Lett 38:L09317. https://doi.org/10.1029/2011gl047147
Ruiz S, Metois M, Fuenzalida A, Ruiz J, Leyon F, Grandin R, Vigny C, Madariaga R, Campos J (2014) Intense foreshocks and a slow slip event preceded the Iquique 2014 Mw 8.1 earthquake. Science 345:1165–1169. https://doi.org/10.1126/science.1256074
Ruiz S, Klein E, del Campo F, Rivera E, Poli P, Metois M, Vigny C, Baez JC, Vargas G, Leyton F, Madariaga R, Fleitout L (2016) The seismic sequence of the 16 September 2015 Mw8.3 Illapel, Chile earthquake. Seismol Res Lett 87:789–799. https://doi.org/10.1785/0220150281
Takamatsu N, Miyazaki T, Ohno K, Murakami S, Wakasugi T, Ohta Y (2024) Rapid estimation of coseismic crustal deformation and fault model associated with the 2024 Noto Peninsula earthquake using REGARD. In: Abstract of Japan Geoscience Union Meeting 2024: U15-P63, Chiba, Japan, 26–31 May 2024
Twardzik C, Das S, Madariaga R (2014) Inversion of the physical parameters that control the source dynamics of the 2004 Parkfield earthquake. J Geophys Res 119:7010–7027. https://doi.org/10.1002/2014jb011238
Uemura K, Ide S, Aochi H (2023) Influence of rupture velocity on dynamic nucleation. Earth Planet Space 75:123. https://doi.org/10.1186/s40623-023-01866-9
Yamada T, Ohta Y, Nishimura T, Hiramatsu Y Kinoshita Y, Yoshida K (2024) Relationship between the coseismic slip distribution and its assumed fault geometry in the 2024 Noto Peninsula earthquake derived from very dense geodetic observation data. In: Abstract of Japan Geoscience Union Meeting 2024: U15-P65, Chiba, Japan, 26–31 May 2024
Yoshida K, Uchida N, Matsumoto Y, Orimo M, Okada T, Hirahara S, Kimura S, Hino R (2023) Updip fluid fluid flow in the crust of the northeastern Noto Peninsula, Japan, triggered the 2023 Mw6.2 Suzu earthquake during swarm activity. Geophys Res Lett 50:e2023GL106023. https://doi.org/10.1029/2023GL106023

Publisher's Note